Measuring Diffuse, Direct, and Global Irradiance Using a Sky Imager

Benjamin Kurtz[a,*], Jan Kleissl[a]

[a] *Center for Renewable Resources and Integration, Department of Mechanical and Aerospace Engineering, University of California, San Diego, United States*

Abstract

Sky imaging systems are commonly used for aerosol characterization, cloud detection, and solar forecasting. We present an algorithm for measuring full-sky radiance with a range that exceeds the normal dynamic range of the camera system in question. Extended dynamic range over most of the sky is achieved with multiple exposures and High Dynamic Range (HDR) imaging, while solar beam intensity is estimated using CCD smear. Smear measurements are calibrated to match reference GHI based on pixel position on the sensor, and resulting irradiance measurements are validated. Global horizontal irradiance RMSE (root-mean-square error) for a year-long data set is in the 9–11 % range for per-image data and 6–9 % for hourly-averaged data when compared against a solid-state pyranometer. In addition, Direct Normal Irradiance (DNI) measurements for clear skies during a five-month period are compared to a non-co-located SPN1 DNI sensor, with RMSE of 8 %.

Keywords: irradiance, whole sky imager, CCD smear, DNI

1. Introduction

Global horizontal irradiance (GHI) and direct normal irradiance (DNI) are two essential parameters in solar resource assessment. GHI is the standard measure of total available solar radiation, and is typically measured using a

*Corresponding author: B. Kurtz
Email address: bkurtz@ucsd.edu (Benjamin Kurtz)

thermopile or photodiode pyranometer. DNI is the intensity of the direct solar beam and is the portion of the solar resource used by concentrating solar technologies; it is also important for calculating total irradiance on a tilted plane. DNI measurement is typically accomplished using a pyrheliometer on a solar tracker. Radiation coming from the rest of the sky, diffuse horizontal irradiance or DHI, can be measured by shading a pyranometer with a shade ball mounted on a solar tracker [1]. Measurements of GHI, DNI, and DHI made with high-quality, well-maintained instruments have 95 % confidence intervals around ± 2 % for DNI and from ± 3 % to ± 10 % for GHI, depending on the solar zenith angle [1]. Researchers at the National Renewable Energy Laboratory (NREL) find that compared to standard-class reference measurements of GHI, thermopile pyranometers have 1-hour RMSE between 1.5 and 5 % depending on the configuration (ventilation, thermal corrections, etc), while silicon-based pyranometers such as the LI-200 have 1-hour RMSE of 3.5 % [2]. Accuracy of silicon-based sensors can be improved by correcting for their angular and spectral response. For precise angular measurements, scanning radiometers or spectroradiometers have narrow fields of view and can be positioned at will to sample radiance from various parts of the sky.

Alternative techniques intended to have lower upfront and maintenance costs are often proposed. Rotating Shadowband Irradiometers (RSIs) are devices that have a single pyranometer and a rotating shadowband to measure both GHI and DHI from which DNI can be computed. Typical 95 % confidence intervals for the resulting DNI measurement are around ± 5 % [1]. However, the single axis of rotation and the typical use of a diffuser rather than an optical dome mean that RSIs are much less sensitive to maintenance schedules [1]. Another approach, taken by the SPN1 sunshine pyranometer, involves measurements using seven miniature thermopiles underneath a complex shading dome. The shading dome is constructed so that for any sun position, at least one sensor is fully shaded and at least one is fully exposed, so that in principle direct and diffuse components of the irradiance can be calculated. This eliminates moving parts, but has been found to result in a systematic positive bias in DNI measurements of $1.1 - 4.1$ %

with 1-minute RMSE of 8 to 14 % even after advanced calibration as reported in Badosa et al. [3]. An NREL study found that the SPN1 had reasonable MBE (mean bias error) and RMSE (of 3 % and 5 %, respectively) on 1-hour GHI, but larger errors (MBE 7.2 % and RMSE 9.5 %) on 1-hour DNI [2].

There is a long history of using cameras to measure the brightness pattern of the sky. They have an advantage in angular resolution over hemispherical sensors, and an advantage in speed over scanning radiometers. As early as 1970, film cameras [4] and later CCDs [5, 6] were used to measure the sunshapes - the normalized azimuthal average profile of broadband radiance about the sun. Techniques generally involve imaging the sun through one or more dark filters to bring it in range of the camera, and researchers were generally concerned only with relative brightness. However, Kaluza and Neumann detail the use of a CCD in concert with a flux gauge to produce absolute readings [7]. A modern commercial device called the Sun and Aureole Measurement system uses two cameras with different filter settings to image a larger region around the sun, and can be calibrated using a sun photometer to give absolute radiance as well [8]. On the wide angle front, many researchers over the years have used fisheye lenses to measure the radiance distribution of the sky [9, 10, 11, 12, 13], generally with absolute calibrations, but the direct beam is generally either blocked or saturated and therefore not measured, although Tohsing et al. estimated the direct beam at either its clear-sky value or 0 depending on whether the sun was obscured by clouds [13]. Several of these researchers were interested in luminance distributions (weighted for the human visual spectrum) for daylighting applications rather than solar energy production, but the procedures are much the same.

More recently, as whole-sky cameras have become common tools for solar energy forecasting, a few groups have extracted image features (such as textures, colors, and cloud coverage [14] or cloud locations [15]) to build empirical models for GHI and DNI without trying to measure the exact spatial distribution of radiance.

We propose a system that allows the use of a camera system described by

Urquhart et al. [16] (the UCSD Sky Imager, or USI) to measure both DHI and DNI based on the photon fluxes incident on the image sensor. This physicality differentiates our method from those which rely on an image classification layer [14, 15], while our ability to make a non-binary determination of DNI is an improvement over radiance-based methods [13]. After introducing our data sources (section 2), we proceed with a discussion (section 3) of the methods used to measure and calibrate irradiance, with particular emphasis on the technique we have developed for measuring DNI using CCD smear. We then compare these results against LI-200 GHI and SPN1 DNI measurements (section 4) and show good qualitative and quantitative agreement. Finally, we conclude (section 5) with some ideas for improvement and additional applications.

2. Data

USI images for this study were captured every 30 seconds during daylight hours beginning on August 18, 2014 and ending on August 17, 2015. Data points corresponding to sun positions less than 20 pixels (2.5°) above the obstructions on the horizon were omitted in order to ensure that both the reference sensor and the USI were unaffected by said obstructions.

The reference GHI sensor, used for both calibrations and validation, is a LI-COR LI-200 silicon pyranometer located approximately 10 m from the camera. Reference data points are 3-second averages of 20 Hz samples centered at the time of the image. The data logger was intermittently overloaded with data acquisition instructions, and occasionally dropped up to a few minutes worth of data. Additionally, there were a few periods of longer downtime. In total, 15 % of 3-second average data points at times corresponding to camera images were missing from the data set.

In April 2015, a Delta-T SPN1 sunshine pyranometer was added on a rooftop 1.25 km from the camera in order to be able to compare DNI and DHI as well. The SPN1 uses seven miniature thermopiles and a complex shading mask to measure both GHI and DHI, from which it calculates DNI. Data is sampled

at 1 Hz. However, these validation data presented issues due to the spatial displacement. Purely random differences in high resolution data due to spatial displacement could be reduced by temporal averaging, but in this coastal climate (1 km from the ocean) systematic differences in cloud cover exist with a bias towards more cloudy conditions near the ocean. While these clouds are typically thin and do not significantly affect GHI, DNI differences can be large. Since occasionally different cloud conditions persist for several hours these data are therefore suitable for quantitative comparisons only during time periods that are cloud-free. While differences in aerosol loading between the two sites could also change the partition from GHI to DNI, the strong sea breeze flow typically causes air masses of oceanic origin to exist at both sites.

3. Methods

We will decompose GHI into three separate components to be extracted from each set of images.

$$\mathrm{GHI} = \mathrm{DHI}_{\mathrm{raw}} + \mathrm{DNI} \cdot \sin(\alpha) - \mathrm{DHI}_{\mathrm{stray}}, \tag{1}$$

where α is the solar elevation above the horizon. The raw measurement of DHI will be derived from most of the pixels in the 16-bit high dynamic range (HDR) image captured by the camera described in Urquhart et al. [16]. Three images with adjacent exposure times varying by a factor of 4 are combined by averaging pixel readings exposed in the linear range of the detector. Unfortunately, without a filter changer, the camera does not have enough dynamic range to capture the intensities in the solar region directly—the sun is at least 15 times as bright as the brightest object the camera can record at its shortest exposure time. Therefore, pixels near the sun are always saturated when the sun is unobscured. DNI will be measured instead by measuring the intensity of CCD smear that results from the presence of very bright light sources such as the sun. As smear occurs during readout, it is expected to be independent of exposure time. This can lead to complications in the HDR compositing process which expects

pixel values to scale with exposure time. For this reason, a single exposure at the camera's shortest exposure time (75 μs) is used for smear measurement. The short exposure time enhances the brightness of smear relative to the rest of the image. Finally, DHI is corrected downward to account for stray light that is scattered off the camera optics when they are illuminated by direct sunlight. Note that the stray light correction does not have to be added back to the DNI measurement since the DNI method utilizes a scaling factor that is also expected to correct for stray light losses to the DNI signal.

Although insufficient to measure the direct solar beam, the dynamic range of the camera is generally sufficient to capture the remainder of the sky scene with a fixed set of exposures under all sky conditions. This simplifies the conversion from pixel values to radiance. Capture time for the sequence of four images (three for HDR plus a minimal-time exposure) is approximately 830 ms, of which roughly 200 ms is delay between frames.

All three components of Equation 1 require calibration in order to provide values in meaningful physical units. While optical setups could be calibrated in the lab, small changes in focus and alignment can lead to nontrivial changes in calibration factors; our objective is therefore to present an algorithm that can be self-calibrated using field measurements.

3.1. Diffuse Irradiance from HDR Image

Methods for absolute radiance calibration of the camera are fairly standard and are presented by other researchers [9, 13]. Essentially, a uniform, calibrated, Lambertian reflectance plaque is illuminated by a calibrated light source, and the distance from the source to the plaque is varied along with the camera exposure time, thereby recording the mapping from pixel values v and exposure times t into radiance L. DHI is then a straightforward sum of the product of radiance, cosine of the angle of incidence θ, and solid angle $\delta\Omega$ over all pixels above the horizon and outside the direct beam region (typically between 2 and

5 degree radius from the sun, depending on the desired characteristics).

$$\mathrm{DHI}_{\mathrm{raw}} = \sum_{\text{sky hemisphere}} L(v,t)\cos\theta\,\delta\Omega \tag{2}$$

However, under many circumstances, a precise radiance calibration for a given instrument will not be available. Even a lab calibration alone may not be enough, as the relative position of the lens and the sensor may change slightly during camera deployment. When an accurate field calibration is unavailable, the pixel's radiance L is assumed to be linearly proportional to the pixel value v and exposure time t. Previous work has found pixel brightnesses to be linear within 10 % for this camera [16]. The proportionality constant β typically has a small spatial variability due to nonuniform pixel sensitivity and optical effects. Pixel sensitivity is generally small and in any case varies from camera to camera. On the other hand, rolloff (the decreased transmission of the optics with increasing view-angle, sometimes known as vignetting) is primarily a function of the optics and the distance from the optical axis and is expected to be comparable between cameras of the same model and optical configuration. Radiance is therefore approximated as

$$L(v,t) = \beta_0\beta'(r)vt, \tag{3}$$

where β_0 is now a constant across the image (assuming homogeneous pixel sensitivity) which can be estimated using reference GHI data. $\beta'(r)$ can be measured by capturing images under uniform illumination (e.g. several rotations of an integrating hemisphere). In the event that measurements for $\beta'(r)$ are unavailable, it is expected that reasonable results could be obtained taking $\beta'(r) = 1$ independent of r (i.e. assuming rolloff is negligible). Thus, a range of accuracy levels can be achieved, depending on the calibration equipment available: fully calibrated radiance should give the best accuracy, but may be hard to achieve in most scenarios; GHI-calibrated, radially variable response is easier to achieve; and GHI-calibrated constant response requires no extra calibration of the camera, but results may be lower in accuracy. Here, we have taken the second approach, i.e. approximating $L(v,t)$ as indicated in equation

3 with $\beta'(r)$ dependent on r. We note that many low-cost cameras compress pixel values for storage with the result that values are no longer linearly related to brightness; users of such cameras may require extra steps to recover radiance from pixel values.

To determine β_0, DHI is calculated during times when DNI and therefore stray light contributions in equation 1 are expected to be nearly zero. β_0 is then determined using a linear fit against data from a nearby GHI sensor (see Fig. 11 later for an example). In our experience, one day with at least 40 % low-DNI conditions is sufficient for the determination of β_0. Low-DNI conditions can be conveniently defined in this context as (i) average pixel brightness in the solar region ($< 2.5°$ from the sun) is less than 2.5 times the average pixel brightness outside the solar region, (ii) raw DNI (h from equation 6 below) is nearly zero, specifically h is less than 1 % of the 98th percentile, and (iii) reference GHI is between 75 and 250 W/m^2. The first condition ensures that the difference between DHI and GHI is less than about 0.25 %, which the second confirms by checking that measured DNI is low. The third condition avoids low solar elevations as well as bright and dark conditions in which nonlinearities were observed.

A standard pyranometer measurement includes the influence of any obstructions to its field of view. To replicate those conditions, we have opted not to mask trees and distant structures along the horizon before summing diffuse irradiance. However, an advantage of camera-based radiance measurements is that such obstructions can be removed if desired. Masked regions could then be filled with the average value from the rest of the sky, or with values interpolated from nearby portions of the sky using an appropriate model for anisotropic diffuse radiance.

The spectrum of DHI is markedly different under clear and overcast skies. It is therefore advisable to use a weighted combination of the different color channels in order to obtain a desired spectral response. Thermopile pyranometers are typically designed to have uniform spectral response (measurement of 1 W/m^2 is independent of the spectral content of the radiation). However, for

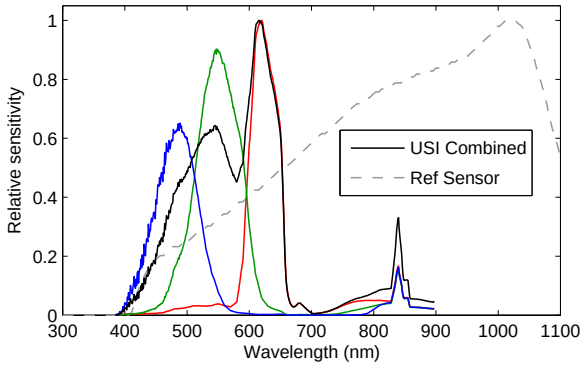

Figure 1: Red, green and blue lines illustrate the relative spectral sensitivity of the associated color channel in the USI image sensor [17, 18]. For comparison, the effective combined (RGB weights 1, 0.65, 0.5) sensitivity for DHI is shown in black, along with the sensitivity of the LI-200 reference instrument (dashed gray) [19].

some resource assessment applications, it may be desirable to select weights to match a particular instrument or a specific model of photovoltaic device. For the camera used in this study, weighting factors of 1 for red, 0.65 for green, and 0.5 for blue were found to provide the best match to the reference sensor (based on a linear least-squares fit of the spectral response in the 400-700 nm range where the camera has significant sensitivity), as illustrated in Figure 1.

3.2. Stray Light Correction

Previous work found stray light to contribute as much as $10 - 20$ % of the observed radiance in some areas of the image [16]. Therefore a correction term was introduced in Eq. 1. Stray light is assumed to be due only to reflections and scattering of the direct beam in the optics. In the general case, we expect that the amount of scattering might depend on solar elevation, α, due to changes in angle of incidence and intersected area. We shall refer to the ratio of stray DHI to DNI as the *stray fraction*, S:

$$S \equiv \frac{\mathrm{DHI}_{\mathrm{stray}}}{\mathrm{DNI}} = S(\alpha) \tag{4}$$

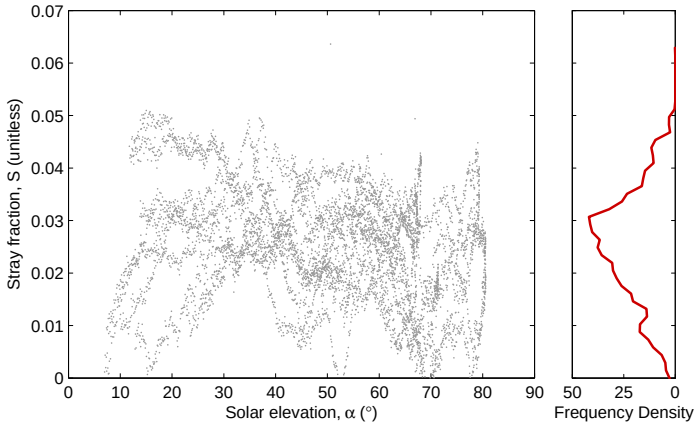

Figure 2: Difference between $\mathrm{DHI}_{\mathrm{raw}}$ and $\mathrm{DHI}_{\mathrm{SPN1}}$ as a fraction of DNI for several clear days between April and July 2015. The red line at the right indicates the frequency of a given stray fraction across all solar elevations. Strong dips (e.g. at $\alpha = 70$) arise from times where no single SPN1 sub-sensor is completely unshaded.

Although there is potential for a more complex relationship between stray fraction and solar elevation, Figure 2 indicates that the camera used in this study does not exhibit any appreciable relationship at all, i.e. $S(\alpha) = \text{const}$. We suspect that this is not true for all cameras.

One potential issue with modeling stray light as a function of DNI is that localized areas of strong scattering in the optics—for example, scratches, smudges, or dirt—tend to cause increased stray light while simultaneously resulting in a lower DNI measurement due to the increased attenuation. As this effect is similar to that of passing thin clouds, it is nontrivial to correct for, and we do not attempt to do so in this work.

3.3. Direct Beam Estimation

3.3.1. Smear and blooming in CCD sensors

As DNI of 5 $\mathrm{W/m^2}$ is sufficient to saturate pixels in the solar region, it is impossible to measure the direct beam radiance directly using pixel values. Instead we turn to the smear effect of CCD sensors. In an interline-transfer CCD such as is used in the USI, charges are collected in a capacitor-like potential well

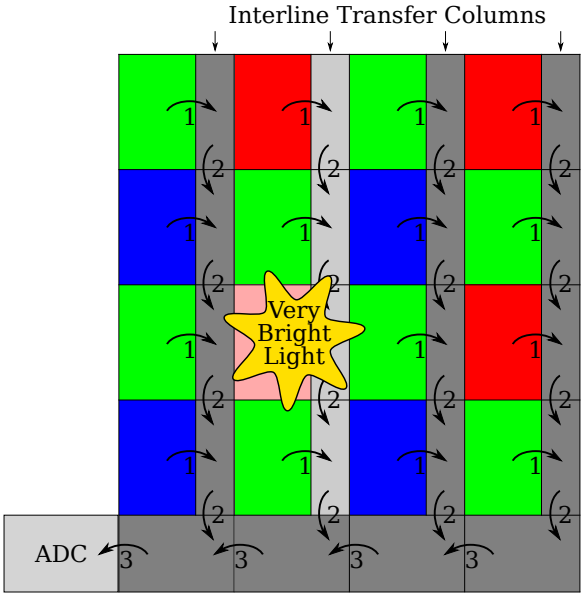

Figure 3: Illustration of smear at the sensor level. Colored rectangles represent light-sensitive pixels of various colors, while gray rectangles indicate regions of the sensor behind a light-blocking mask. The CCD readout process first shifts charges into the interline transfer column (1), then shifts them down to a horizontal shift register one row at a time (2), and finally off the chip into the A/D converter (3), repeating 3 and 2 as necessary until all pixels have been read. Smear is introduced when photons or electrons from a brightly illuminated pixel leak into adjacent interline transfer pixels. The extra charges join those already collected for each pixel in the column as the original charges move past the brightly illuminated pixel.

at the site of each pixel during integration, and then shifted off of the chip into an A/D converter. Charges are shifted into and then down a so-called "interline transfer" column (illustrated in Figure 3), which is behind a mask to prevent additional light from changing pixel values during readout. However, in the presence of very bright light, some photons or excess electrons can still overflow into the interline transfer column during readout, causing smear. Note that as smear occurs during readout, the intensity of the smear effect will depend on frame readout time, rather than exposure time. For a review of CCD operation or more details on smear, readers are referred to [20, 21].

Smear is often accompanied by another effect known as blooming, which

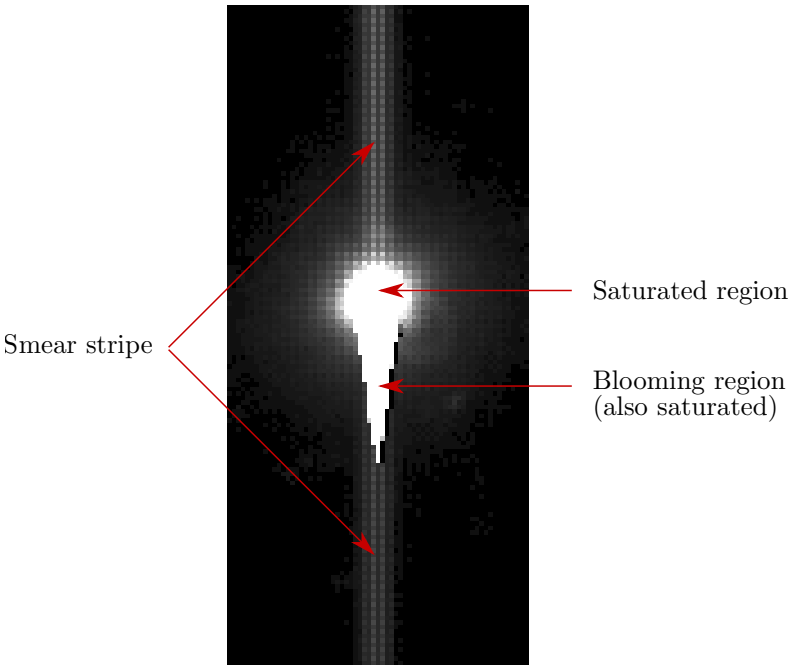

Figure 4: Solar region (67 × 147 pixels) of a 75 μs exposure exhibiting blooming and smear. Blooming is the overflow of CCD cells into neighboring cells, resulting in a pointy "tail" on the sun. Smear results in excess signal penetrating the interline transfer columns, which brightens the entire column as charges are shifted off the chip to the A/D converter.

describes pixels that overflow into their neighbors during the exposure. These effects are illustrated in Figure 4. Blooming is difficult to separate from the saturation in the solar region, whereas smear extends through the entire column, making it easier to measure.

3.3.2. Smear intensity

In order to separate the smear from the rest of the image, we calculate the average value of each column, and then look for columns that have elevated values in comparison with those nearby. Removing 5 to 10 % of the rows immediately around the sun reduces the influence of the saturated portion of the image on the column-average values. Additionally, some rows need to be removed due to side-effects of hardware cropping (discussed in Appendix A.1) of

the image.

Rows are therefore removed from about 300 pixels above to 200 pixels below the position of the sun. When there are saturated pixels in the image, the sun is taken to be at the center of the saturated region; otherwise, a modeled sun position is used, based on the geometrical calibration procedure described by Urquhart et al. [22]. If neither a calibration nor saturated pixels are available, sun position can be approximated based on the brightest pixels in the image.

Note that when taking column averages, it is important to separate the color channels of the image, as they are apparently affected differently. More specifically, half of the columns of the image contain red and green pixels, while the remainder contain green and blue as shown in Figure 3. Red filters have the highest transmissivity and blue the lowest, so alternating columns experience different amounts of smear. For reasons that are not well understood, the red pixels also exhibit higher smear than the green pixels in the same column, though the green and the blue in the other column are nearly the same as might be expected given that they share the same interline transfer column (see Appendix A.2). We have opted to work primarily with the red pixels, as they exhibit the highest smear signal on the lowest background, since Rayleigh scattering is weakest for longer wavelengths (the sky is blue). Our feeling is that the reduction in error realized by a more careful consideration of spectral effects is likely to be small in comparison with the improvement from resolving outstanding difficulties with the DNI calibration procedures.

Next, the location and magnitude of the stripe are determined. The coarse sampling (only every second column contains red pixels, see Figure 3) and nonzero background (natural variation of red irradiance across the image) mean that using the maximum point of the column-wise average signal $\overline{v_x}$ is incorrect. Instead, taking the cross-correlation of $\overline{v_x}$ with a Gaussian template (kernel) yields a robust pattern-matching metric (Figure 5).

$$h^\star(x_0) = \sum_{x_0-19<x\leq x_0+19} \overline{v_x} \cdot \Big(T(x-x_0) - \langle T\rangle\Big) \tag{5}$$

Here, $T(x) = \exp(-x^2/2\sigma^2)$ is the Gaussian template, which has mean $\langle T\rangle$ over

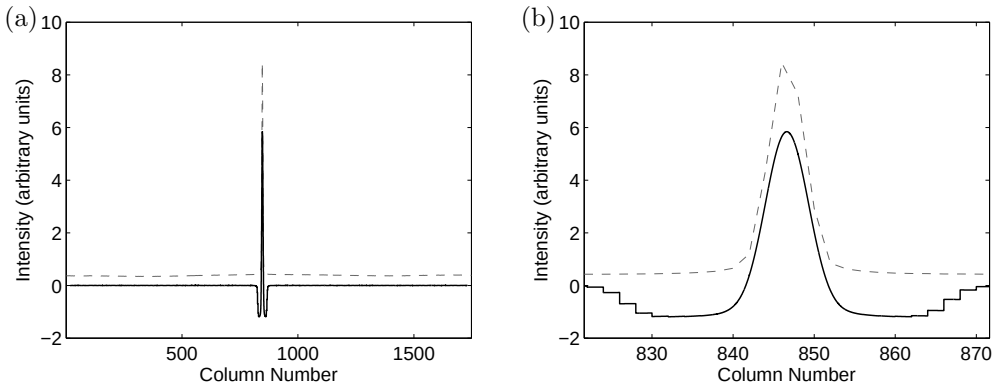

Figure 5: Column means for (a) all columns and (b) columns near the smear stripe, of the red channel before (dashed gray line, $\overline{v_x}$) and after pattern matching (solid black line, $h^\star$) with a 1.07 pixel Gaussian template as defined in Eqns. 5 and 6.

the range of x. A template width of $\sigma = 1.07$ pixels with a window size of 39 pixels (20 red pixels) was empirically chosen.

Figure 5 shows column-wise means of the red channel before and after pattern matching. The coordinates of the maximum point in this curve give the smear intensity (h) and the location of the smear stripe.

$$h = \max_{x_0}(h^\star) \tag{6}$$

Note that $h^\star(x_0)$ can be evaluated for non-integer x_0.

3.3.3. Calibration

The computed smear intensity, h, should be proportional to DNI, however as sensor manufacturers typically design to avoid smear rather than provide consistent smear, sensitivity and linearity vary considerably over the image. We expect the magnitude of the smear effect to depend on the location of the pixel on the sensor. This may be due, for example, to spatial differences in pixel sensitivity, and differences in the alignment of the metal mask covering the sensor. We also expect that there may be some variation with solar elevation, which affects various angles of incidence and the path length through the optics.

The raw smear intensities h therefore need to be calibrated to yield DNI.

We begin by applying the same $\beta'(r)$ roll-off correction discussed for DHI, but an additional calibration factor (C) is required.

$$\mathrm{DNI} = C(x,\alpha)h' = C(x,\alpha)\beta'(r)h \tag{7}$$

$C(x,\alpha)$ are determined by one of two methods, and then the roll-off-corrected smear intensity h' is multiplied by the calibration factor to yield DNI. The simpler of the two methods is to assign a fixed calibration to each column ($C(x)$) based on a look-up table. The more complicated method also takes into account the elevation angle for each pixel ($C(x,\alpha)$), and uses an artificial neural network (ANN) for obtaining the relationship. The advantages of the simple method are its ease of implementation and predictable behavior for data outside the training period. The ANN generally produces better DNI values when interpolating within the range of solar elevations covered by the training data, but may not be reliable outside.

$C(x,\alpha)$ is trained using data from several clear days. Predominantly clear days were selected by manually screening a GHI time series, followed by removal of short cloudy periods by visual inspection of images. As clouds will cause significant disturbance in the calibration factors, a cursory inspection of calibrated results helps confirm that clear training data was used.

As a reliable source of DNI is not generally available to calibrate against, linearity of smear response is assumed and calibration is performed against the residual GHI after DHI (including stray light) is accounted for:

$$\mathrm{DNI}_{\mathrm{nom}} = \frac{\mathrm{GHI} - \mathrm{DHI}_{\mathrm{raw}}}{\sin(\alpha) - S}, \tag{8}$$

where the GHI measurement here is taken from the reference sensor, while DHI comes from the camera. If available, data from a nearby well-maintained DNI sensor would be preferred and could alleviate the requirement of an empirical model for stray light, but such a sensor with sufficient data quality was not available for the present study.

Calibrations were found to change significantly when camera focus or other optics were adjusted, so the year of data was divided into three periods for cali-

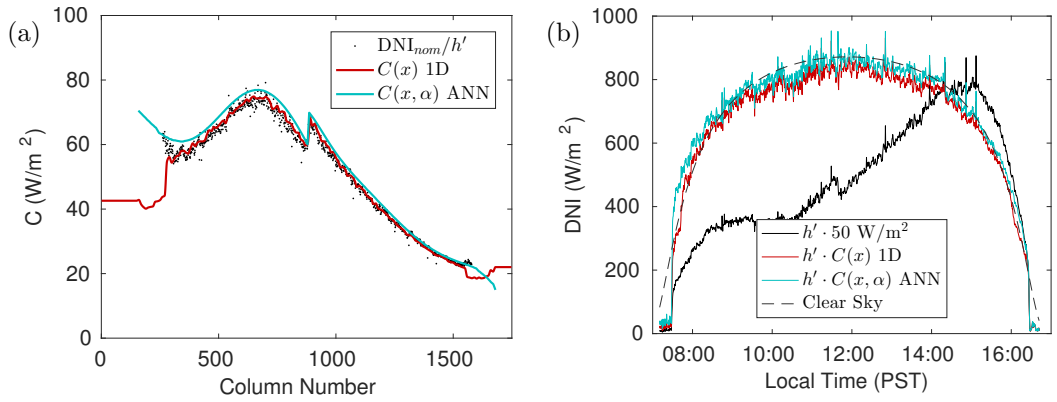

Figure 6: (a) Calibration factors (Eq. 7) and (b) DNI on a clear day (January 3, 2015) before and after calibration using a 1D lookup table (as a function of image column) and a neural network (which considers image column and solar zenith angle). On this day, squared errors are below average and bias errors are larger than average for both the ANN calibration (RMSE 4.5 %, MBE 3.9 W/m^2) and the 1D lookup table calibration (RMSE 2.3 %, MBE -7.0 W/m^2).

bration, as documented in Appendix B. Example values of C as well as fits using both methods for one day are illustrated in Figure 6a. For comparison against the results in Section 4, the figure lists errors calculated using the standard metrics defined in Appendix C.

The lookup-table based method estimates C from x alone. Training data are placed into 10-pixel bins in x, and the median value of each bin is used for the lookup table. Cubic spline interpolation in x is used between bin centers, and nearest neighbor extrapolation is applied to x below or above those present in the training data.

The ANN is implemented using MATLAB's neural network toolbox (`fitnet`) with a single 5-node hidden layer and is trained using Bayesian regularization (`trainbr`). Standard procedure for training neural networks is to divide the calibration data into a *training* set and a *validation* set. The error is minimized over the training set, while the validation set is used as an independent measure of the error, which avoids overfitting by allowing training to stop before the minimum error is reached on the training set if validation set errors are

increasing. In order to preserve the independence of the validation set, data from a given day are placed in one of the three sets (training, validation, testing). Specifically, in this case, the first two and last two clear days (generally the days with the highest and lowest solar elevations at solar noon) in each calibration period were placed in the validation set, while the remaining days were divided evenly between the training and testing sets. The ANN is trained 10 times with random starting weights, and the network with lowest errors on training and validation days combined is selected as the final calibration model. Since the USI employs separate A/D converters for the right and left sides of the sensor, there is a discontinuity in $C(x)$ near the center of the image. As a result, separate ANNs are trained for the left and right halves of the image.

The 1D lookup table method is less sensitive to the selection of clear days than the ANN-based algorithm. Nevertheless, best results are obtained if the clear days selected span the full range of seasons; of particular interest are long summer days which potentially provide data for a wider range of x values than shorter winter days. For comparison purposes, we chose to train the lookup table method using the same clear days that were used for the training and validation sets for the ANN.

Sample calibrated results are shown in Figure 6b, along with DNI from the clear sky model of Ineichen and Perez (PV Lib implementation) [23, 24]. While the raw data do not correspond to a typical DNI signal, the calibrated data follow the clear-sky DNI with an RMSE of about 5 %. About one sixth of the RMSE is due to short-term random fluctuations from localized variations in the optics.

3.4. Validation

GHI data during the study year are compared at all times when the sun is more than 20 pixels (approx. 2.5°) above the horizon and data are available from both the camera and the reference sensor, leaving a total of 424,033 images for comparison. Of these, 47,122 were used for calibration and validation, leaving 376,911 images for testing. RMSE and MBE against the reference sensor are

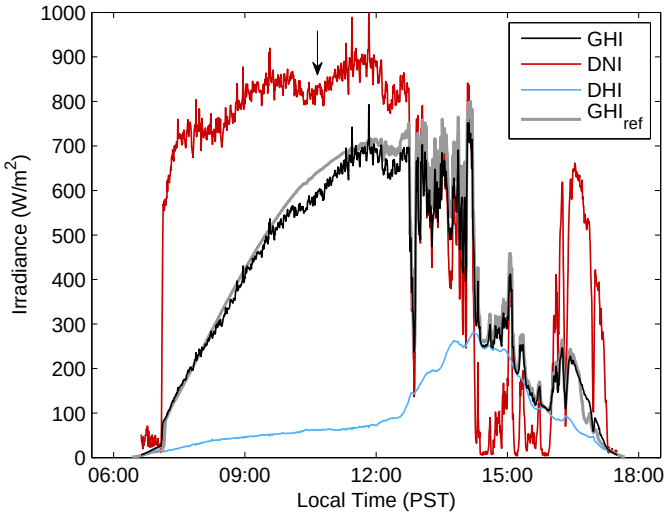

Figure 7: Results for a typical day, 2015-02-11, with the ANN calibration. GHI on this particular day exhibits slightly-below-average RMSE (8.1 %) but has worse-than-average negative bias (−5.6 %). Inconsistencies in the DNI calibration give rise to the dip (indicated by an arrow) in the DNI curve at 10:30 PST and contribute significantly to the negative bias.

computed using the standard definitions, given in Appendix C for completeness.

As previously mentioned in Section 3.3.3 and enumerated in Appendix B, calibration was performed in three separate periods due to optical configuration changes. However, errors were similar across all three periods and are reported without reference to a particular period.

4. Results

Figure 7 shows example results from a partly cloudy day. The camera-derived GHI generally follows the reference sensor, increasing as the sun rises above the horizon in the morning and then dropping steeply as clouds move in in the afternoon. Of particular note is the accuracy with which the camera follows the steep drops that result from shading of the direct beam. However, this example also illustrates several of the most prevalent sources of error. Although reference DNI measurements are unavailable for this day, conditions are essentially clear until 11:00 PST. This would normally suggest a relatively smooth

DNI curve, which is not observed. In actuality, there appears to be significant random noise and a drop in DNI appears around 10:30 PST, both of which are carried over to GHI as well. Inspection of the raw smear intensity and calibration signal reveals that while the dip in DNI around 10:30 PST originates in the smear intensity, on other nearby days (including the two nearest clear days used for calibration), this dip is smaller and is properly corrected. For unknown reasons, some days (including 2015-02-11 and the second clear day before it) have a larger dip in smear, which in this case leads to poor performance even after calibration. Analogous errors on other days can lead to positive bias in DNI as well. Meanwhile, the increased noise in the camera's DNI measurement arises primarily from localized optical defects. When target calibration factors are displayed as a function of image position, some of these optical defects can be visually associated with dirt and scratches on the dome. To verify that noise is not caused by the sensor, for one day a burst of 10 images was taken within 0.7 sec rather than a single image every 30 sec. For each set of 10 images, the path through the optical system is essentially identical. Over the course of two clear hours, fractional variation of smear intensity within a burst of images was only 0.15 % to 0.6 % compared with 12 % for images that were 30 seconds apart. Finally, DHI measurements are too small during times of high diffuse; on this day, this can be seen most clearly shortly before 15:00 PST when DNI ≈ 0, but is also demonstrated in Figure 11 later.

Daily error statistics for instantaneous GHI are presented in Figure 8. Errors tend to be lower on and near days used for calibration. Yearly statistics broken down by training and testing are shown in Figure 9a with RMSE for instantaneous GHI around 10 %, and MBE < 2 %. RMSE for 1-hour average GHI is around 7 %. The data generally follow the expected trends that data used for training or cross-validation should have lower errors than testing data, that the neural network should perform better than the 1-D lookup method, and that 1-hour averaging helps reduce errors due to random processes. The relatively small MBE is not surprising as the calibration of both DHI and DNI is based on the reference sensor.

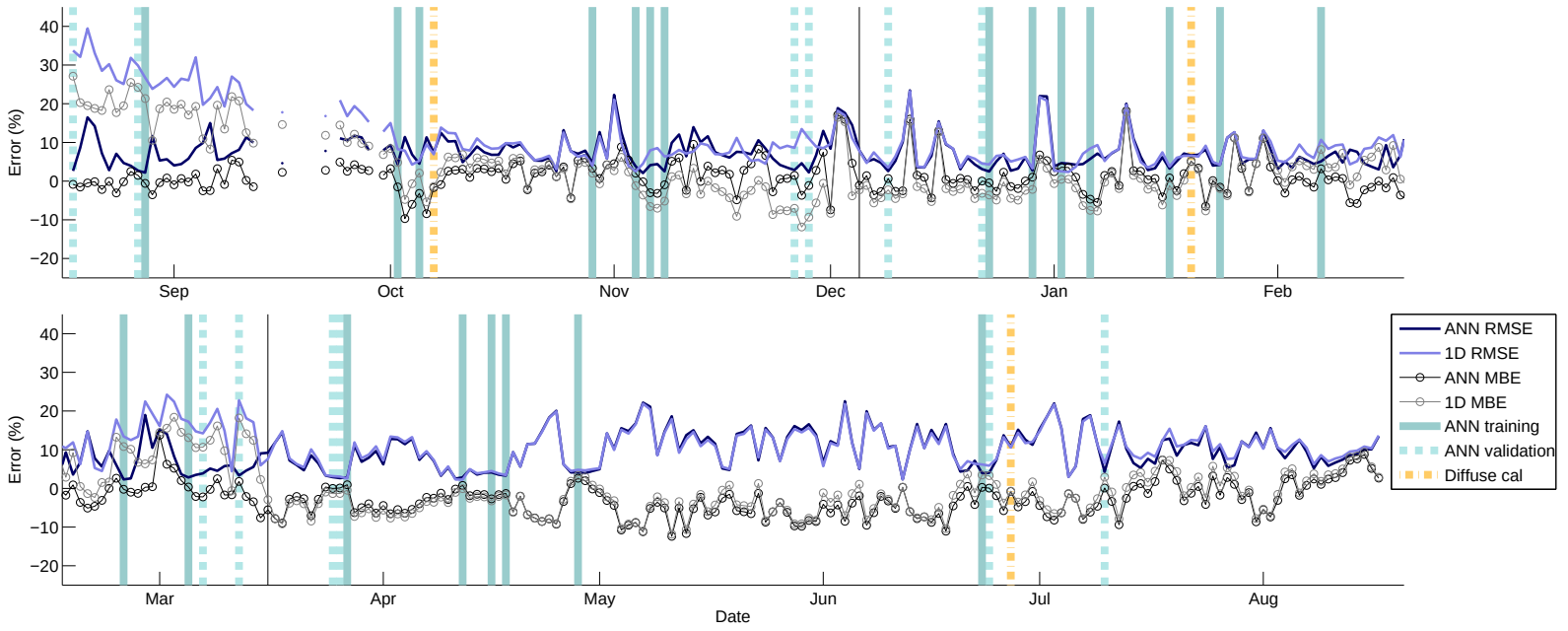

Figure 8: Daily GHI error normalized by daily mean GHI. Colored stripes in background indicate days used for training and calibration. Thin black vertical lines indicate separation between the different calibration periods (see Table A-1). Because the 1D lookup calibration does not distinguish between training and validation, days used for ANN validation are lumped into the training set for the 1D calibration.

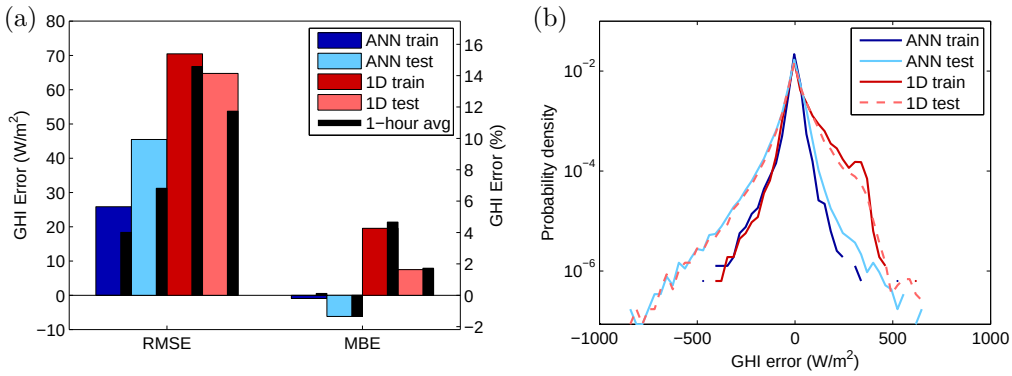

Figure 9: Error statistics for the test data set over the course of approximately one year. In (a), colored bars indicate error rates for instantaneous data, while black bars are for 1-hour averages that are often used in performance simulations. The right axis is scaled to the left axis using the mean of the testing data (cf. Equation 9); therefore the error percentages are not entirely accurate for the training data. Probability densities of instantaneous GHI errors are shown in (b) with the same color scheme as in (a).

A distribution of errors is shown in Figure 9b. Large overpredictions are significantly less common for the ANN calibration than for the lookup table calibration. Both calibrations have similar probabilities for large underpredictions. Figure 10 breaks out errors for low-DNI periods and clear days, which exhibit fewer large errors than the overall data set. However, the error distributions for hourly-averaged data no longer show this distinction; this suggests that many of the large errors may be due to the larger spatial and temporal variability in GHI under partly cloudy conditions, rather than because measurements are inherently better under clear or low-DNI conditions.

The fact that relative hourly errors for low DNI are comparable to other conditions suggests a prominent source of errors in conditions dominated by diffuse. By definition, low-DNI periods have GHI $\approx$ DHI, and therefore can be used to evaluate the quality of the DHI measurement. Figure 11 presents these errors for three different days as a function of GHI. June 27 was the day used to calibrate DHI for this period, and shows both positive and negative errors with no overarching trend. In contrast, data from June 15 and 16 have a strong non-

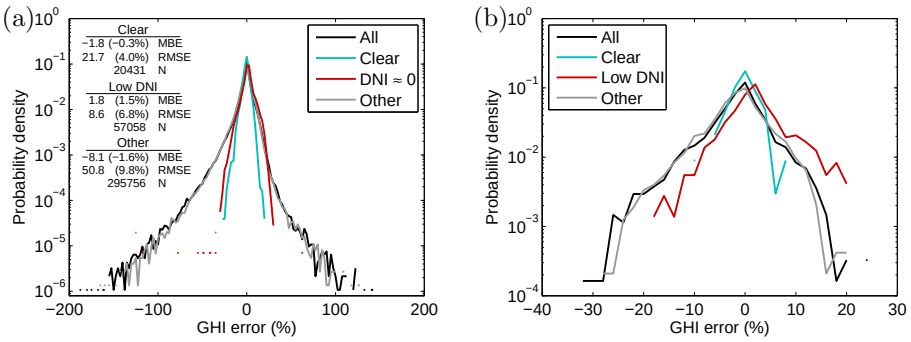

Figure 10: Error distributions for clear and low-DNI conditions, for (a) instantaneous data, and (b) 1-hour averaged data. The black "All" curve in (a) represents essentially the same data as the light-blue "ANN test" line in Figure 9. Low DNI periods are selected using the first two criteria from DHI calibration (no limitations on GHI, see Section 3.1), while clear conditions were determined manually. Error metrics in W/m^2 and image counts are given in (a).

linear trend toward more negative errors with larger GHI, which is also apparent on several other nearby days (not shown). Mornings and afternoons on these days also differ slightly, though not as much as from the conditions on June 27. Some of the error in DHI appears to be related to the difference between spectral channels; for example, on June 27, the errors tend to be positive when the blue channel is brighter than the red, and negative otherwise. However, attempts to correct this by altering the balance between the channels required unphysical combinations with negative weights on at least one channel, and were still unable to remove trends entirely. Some additional spectral mismatch is expected due to the near-zero sensitivity of the USI in the region from 700 to 1100 nm where the reference sensor has significant response (see Figure 1). Additionally, previous work has suggested nonlinearity on the order of 5 % in camera sensitivity, which would lead to errors in DHI measurement without better calibration. Despite these issues, the vast majority (95 %) of these low-DNI periods have errors either < 15 % or < 15 W/m^2.

To validate the DNI performance of the camera, Figure 12 compares the DNI measured by the camera and the SPN1 sensor located 1 km inland. Due to the

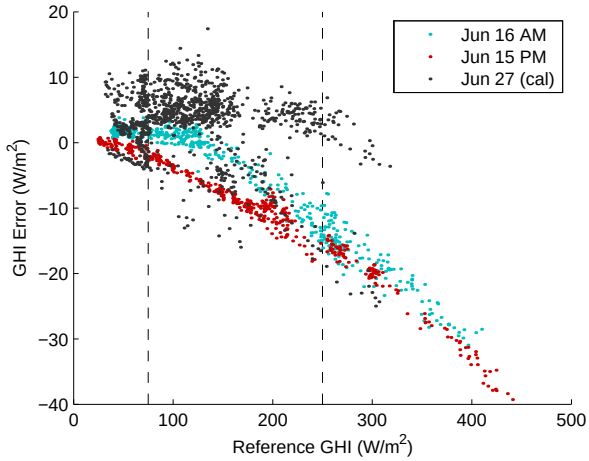

Figure 11: Error as a function of GHI under low-DNI conditions, where GHI ≈ DHI. Data shown are for the ANN calibration. Dashed vertical lines indicate the limits used for DHI calibration on June 27 and two other days (Figure 8).

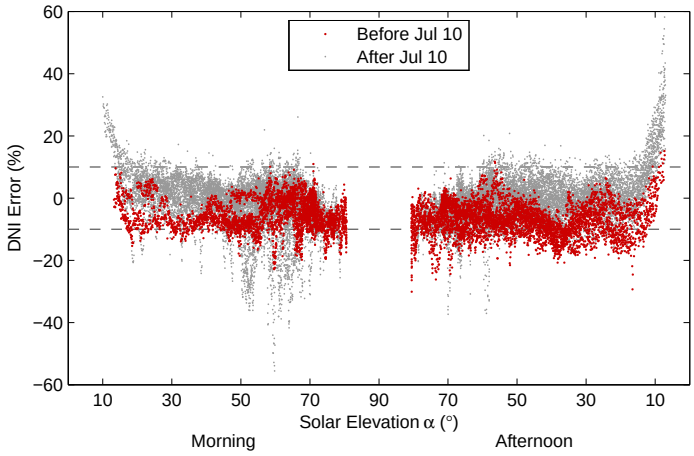

Figure 12: DNI validation of the USI against SPN1 measurements under clear skies. July 10 was the last full clear day used for calibrating DNI measurements, so measurements after that exhibit larger errors, particularly when the sun is low in the sky. DNI errors: RMSE of 66.0 W/m^2 (7.7 %), MBE of −26.0 W/m^2 (−3.0 %). DHI errors: RMSE of 45.4 W/m^2 (53 %), MBE of 41.7 W/m^2 (49 %). GHI errors: RMSE of 51.8 W/m^2 (7.1 %), MBE of 0.2 W/m^2 (0.02 %).

spatial separation between the sites and the proximity to the ocean, the sites are not expected to experience matching DNI in the presence of clouds. To focus on data points where spatially homogeneous conditions prevailed, a reduced set of data from clear periods between April 15 and September 22, 2015 is shown. Because images on these days during these periods were visually observed to be completely clear, both sites should be cloud-free, so that DNI should be comparable. While the measurements generally agree to within 10 %, the USI produces lower measurements on average, except at very low solar elevations where a strong positive bias is present. Additionally, there are several dozen instances of very localized larger negative bias, which were found to correspond to the sun passing behind scratches or dirt on the camera dome. While some of the overall negative bias is likely due to calibration errors in the camera, other researchers [3] have also observed a positive bias between 4.8 and 14 % in DNI measurements from SPN1 instruments due to the min/max procedure used to separate diffuse and direct irradiance. Although it would be possible to calibrate DNI against the SPN1, we are hesitant to do so given its reputation for overestimation of DNI.

5. Conclusions

This paper details the use of an all-sky camera for measuring DNI and DHI from which GHI can be computed. While measuring DHI is relatively trivial by integrating over radiance across the sky hemisphere, the method for measuring DNI is novel and has not been presented before in the literature to our knowledge. Our results confirm that the method is generally effective, albeit with lower accuracy than can be achieved with well-calibrated conventional sensors. However, compared to comparable technologies, accuracy is actually improved. For example, Schmidt et al. [14] report GHI RMSE of nearly 25 % (10-second instantaneous samples) for their image-based method, while Gauchet et al. [15] managed RMSE of 17 % for five-minute average data using cloud position information. Both relative errors are normalized by average daytime irradiance.

However, as errors are generally lower under clear conditions, the comparison of data from different sites does not constitute conclusive evidence as to which method is superior. Different spectral sensitivity of the reference instrumentation further complicates comparisons. These other algorithms generally suffer from limited information about DNI due to saturation in the solar region, and as a result are unable to follow some of the large fluctuations that originate primarily in the direct beam; their performance improves considerably with time averaging (e.g. the algorithm by Schmidt et al. achieves RMSE of 11.7 % on hourly-averaged data). Meanwhile, 1-hour satellite-derived GHI data experiences RMSE from 12 % to 25 % and more, depending on the location [25].

Furthermore, in many cases, the ability to measure radiation using a camera may be useful where only a camera is present. For example, it can simplify data acquisition for a sky-imager based solar forecast [26], since it alleviates the need for a separate GHI data source to assign cloud optical depth. Separating DNI and DHI is also of use when forecasting output from tilted systems, and for determining cloud thickness near the sun where pixels are generally too saturated to contain useful information. Additionally, the ability of a camera to capture the directional dependence of radiance may prove a valuable tool for developing non-isotropic diffuse radiation [27] and transposition [28] models.

The primary source of error in our methodology is expected to stem from the poorly understood relationship between CCD smear intensity and DNI. Although we have derived means of empirically calibrating away these irregularities as a function of pixel position and solar elevation, their exact causes are unknown and it is therefore unlikely that our empirical method captures all underlying relationships and parameters. Furthermore, some observational evidence suggests that smear is nonlinear in intensity (distinct from sensitivity varying spatially), or that smear may not account for all the irradiance typically considered DNI. Indeed, DNI is typically defined to include everything within 2.5° of the sun, but the smear stripe only results from very bright pixels, likely only within the solar disk itself (closer to 0.5°). If the ratio of brightness within the solar disc to brightness within the standard DNI cone remains constant,

then this discrepancy would be accounted for by calibration; however, if the ratio changes as atmospheric conditions change, it would mean that smear stripe alone does not contain enough information to measure DNI. Due to the difficulty of determining the proper ratio in which to combine the two signals, we have elected not to consider the remainder of the solar region or any nonlinearity of smear at this time.

Additional sources of error include variations in the transmissivity of the camera dome due to dust, dirt, and scratches on the outside of the camera dome, but these are expected to primarily result in random errors. Dust and dirt affect all radiation measurement systems, and present special challenges because they change on a daily basis. We have anecdotally observed the camera-measured DNI increasing by several percent on a day when the optics were cleaned. Temperature also affects the camera sensor, but it has a relatively small influence on the value of "normal" pixels, though there is no guarantee this applies to smear.

Although the calibration procedures developed here are general, i.e. they could be applied to any compatible camera, the overall technique places several restrictive requirements on the camera system. In order to capture sufficient dynamic range to measure GHI and DNI, multiple exposures with different integration times are required. In a system with limited dynamic range, allowing the exposure time to respond dynamically to the observed radiation intensity, and using smear from that single exposure rather than a minimal integration should still work; data quality would, however, be expected to be lower. Furthermore, use of dynamic exposure times complicates the conversion between camera measurements and radiance/irradiance. Finally, only certain sensor types actually exhibit smear at all. Indeed, CMOS sensors (which are increasingly common) use in-pixel read-out electronics and therefore are not subject to smear; in fact, CMOS sensors are preferred for sky imaging by some groups because they are immune to smear.

Potential improvements to the method presented in this paper revolve primarily around the DNI calibration procedure. In particular, it would be valuable

to have a field calibration procedure that can eliminate the need to extrapolate DNI calibration factors to different solar zenith angles, and to determine with more certainty which properties of the various calibrations are potentially affected by redeployment or configuration changes of the instrument. Additionally, further automation of calibration procedures would be beneficial, particularly with respect to detection of clear-sky periods. Nevertheless, we expect the correlation between smear and DNI to be robust and applicable to all interline-transfer CCDs, and we expect that in the near future we will make use of this data in our solar forecast algorithm, if not in more demanding resource-assessment applications.

6. Acknowledgements

We acknowledge funding from the California Energy Commission PIER and EPIC programs. Felipe Mejia, Handa Yang, Oytun Babacan, Guang Wang, Andu Nguyen, Bryan Urquhart and Chi Wai Chow are thanked for cleaning and maintaining the UCSD Sky Imager.

Appendix A Extra Camera Details

A.1 Cropping

As mentioned above, hardware cropping is performed in the camera by skipping the A/D conversion step for whole rows. This means that as pixels are shifted off the image sensor, rows immediately adjacent to the sun will have less time to be "contaminated" by smear, resulting in a lower smear signal in these rows.

Empirically, it is observed that cropping the top of the image by N pixels affects the N rows immediately below the sun, while cropping the bottom of the image by M rows affects M rows somewhat above the sun in the following image. The distance above the sun is unfortunately somewhat dependent on time between image captures; in a test data set, it was approximately 130 pixels.

Our current recommendation is to remove the entire region affected by cropping (from 300 rows above to 200 rows below the sun for the USI), or perhaps, better yet, to disable hardware cropping for the exposure used to measure DNI and an extra frame before it, which can be discarded.

Astute readers will note that, since cropping the top of the image affects rows below the sun that this implies that the horizontal shift register is actually located at the top of the image sensor, which is contrary to the way the sensor is drawn in most literature!

A.2 Color Channel Differences of Smear

Since smear results from overflow of signal into interline transfer columns, we would expect the increase in pixel value due to smear to be uniform throughout each column of the image since each image column shares an interline transfer column. Specifically, while smear is expected to be higher in the red/green columns than in the green/blue columns due to higher average filter transmissivity, we do not expect to observe any difference between the two different colors within a column. Although more light will cause smear at the location of the red pixel on the sensor, the signal which is altered could have originated in either a red or a green pixel.

Observed smear signals, in contrast, are highest in red pixels, followed by green pixels in the red column. Blue pixels and green pixels in the blue column exhibit lowest smear, and are both about the same, as is expected. We are unsure as to the cause of this, but would welcome proposals, as they might shed further light on the underlying physics, which might in turn help us to improve our calibration procedures and accuracy.

Appendix B Calibration Periods

Period 1 begins at the start of the study period. The starts of periods 2 and 3 each coincide with attempts to improve image focus. While at least some of the changes in calibration are due to the focus change directly, it is anticipated

603 that accidental changes in alignment between the dome, lens, and camera body
604 could require re-calibration any time the device is opened.

605 The first two and last two days in each "DNI Calibration" set were placed in
606 the validation set for the ANN, while the other listed days were used as training
607 data.

	Period 1	Period 2	Period 3
Start [UTC]	2014-08-18 08:00:00	2014-12-05 19:54:00	2015-03-16 19:10:00
End [UTC]	2014-12-05 19:45:00	2015-03-16 18:40:00	2015-08-18 08:00:00
608 DNI Calibration	Aug 18, 27, 28; Oct 02, 05, 29; Nov 04, 06, 08, 26, 28	Dec 09, 22, 23, 29; Jan 02, 06, 17, 24; Feb 07, 24; Mar 05, 07, 12	Mar 25, 26, 27; Apr 12, 16, 18, 28; Jun 23, 24; Jul 10
DHI Calibration	Oct 7	Jan 20	Jun 27

609 Appendix C Error Metrics

610 Error rates are reported in RMSE (root-mean-square error) and MBE (mean
611 bias error), following their standard definitions:

$$\mathrm{RMSE} = \sqrt{\frac{\sum \left(\mathrm{GHI} - \mathrm{GHI}_{\mathrm{ref}}\right)^2}{N}}, \qquad \mathrm{MBE} = \frac{\sum \mathrm{GHI} - \mathrm{GHI}_{\mathrm{ref}}}{N}, \tag{9}$$

612 where GHI is the sky imager, and $\mathrm{GHI}_{\mathrm{ref}}$ is the reference pyranometer mea-
613 surement, or analogously for DNI or DHI. When RMSE (or MBE) is reported
614 in percent, it has been normalized by the average value of the reference sensor
615 during the same time period:

$$\frac{\mathrm{RMSE}}{\frac{\sum \mathrm{GHI}_{\mathrm{ref}}}{N}}. \tag{10}$$

616 In addition, in some places we report errors for hourly-averaged data. In
617 order to avoid biasing the results for or against hours near sunrise/sunset (which

are much more likely than others to have partial data due to horizon exclusion rules), hours in which 45 or more (of 120 possible when sampling every 30 seconds) data points were missing or excluded from were omitted from the hourly statistics.

References

[1] M. Sengupta, A. Habte, S. Kurtz, A. Dobos, S. Wilbert, E. Lorenz, T. Stoffel, D. Renné, C. Gueymard, D. Myers, S. Wilcox, P. Blanc, R. Perez, Best practices handbook for the collection and use of solar resource data for solar energy applications, Tech. Rep. NREL/TP-5D00-63112, NREL, 15013 Denver West Parkway, Golden, CO 80401 (Feb. 2015).
URL http://www.nrel.gov/docs/fy15osti/63112.pdf

[2] A. Habte, S. Wilcox, T. Stoffel, Evaluation of radiometers deployed at the national renewable energy laboratory's solar radiation research laboratory, Tech. Rep. NREL/TP-5D00-60896, NREL, 15013 Denver West Parkway, Golden, CO 80401 (Feb. 2014).
URL http://www.nrel.gov/docs/fy14osti/60896.pdf

[3] J. Badosa, J. Wood, P. Blanc, C. N. Long, L. Vuilleumier, D. Demengel, M. Haeffelin, Solar irradiances measured using SPN1 radiometers: uncertainties and clues for development, Atmospheric Measurement Techniques 7 (12) (2014) 4267–4283. doi:10.5194/amt-7-4267-2014.
URL http://www.atmos-meas-tech.net/7/4267/2014/

[4] A. Deepak, R. R. Adams, Photography and photographic-photometry of the solar aureole, Appl. Opt. 22 (11) (1983) 1646–1654. doi:10.1364/AO.22.001646.
URL http://ao.osa.org/abstract.cfm?URI=ao-22-11-1646

[5] M. Schubnell, Sunshape and its influence on the flux distribution in imaging solar concentrators, Journal of Solar Energy Engineering 114 (4) (1992)

260–266. doi:10.1115/1.2930015.
URL http://dx.doi.org/10.1115/1.2930015

[6] A. Neumann, A. Witzke, S. A. Jones, G. Schmitt, Representative terrestrial solar brightness profiles, Journal of Solar Energy Engineering 124 (2) (2002) 198–204. doi:10.1115/1.1464880.
URL http://dx.doi.org/10.1115/1.1464880

[7] J. Kaluza, A. Neumann, Measurement of solar radiation with CCD-cameras: Influence of the spectral characteristic, in: Solar Engineering 1998, Proceedings of the International Solar Energy Conference, American Society of Mechanical Engineers, Albuquerque, New Mexico, June 14-17, 1998, pp. 425 – 428.

[8] S. Wilbert, R. Pitz-Paal, J. Jaus, Comparison of measurement techniques for the determination of circumsolar irradiance, AIP Conference Proceedings 1556 (1) (2013) 162–167. doi:10.1063/1.4822222.
URL http://scitation.aip.org/content/aip/proceeding/aipcp/10.1063/1.4822222;jsessionid=8w3amjo3n3sl.x-aip-live-02

[9] J. E. Shields, M. E. Karr, R. W. Johnson, A. R. Burden, Day/night whole sky imagers for 24-h cloud and sky assessment: history and overview, Appl. Opt. 52 (8) (2013) 1605–1616. doi:10.1364/AO.52.001605.
URL http://ao.osa.org/abstract.cfm?URI=ao-52-8-1605

[10] E. G. Rossini, A. Krenzinger, Maps of sky relative radiance and luminance distributions acquired with a monochromatic CCD camera, Solar Energy 81 (11) (2007) 1323 – 1332. doi:10.1016/j.solener.2007.06.013.
URL http://www.sciencedirect.com/science/article/pii/S0038092X07001508

[11] R. Román, M. Antón, A. Cazorla, A. de Miguel, F. J. Olmo, J. Bilbao, L. Alados-Arboledas, Calibration of an all-sky camera for obtaining sky radiance at three wavelengths, Atmospheric Measurement Techniques 5 (8)

(2012) 2013–2024. doi:10.5194/amt-5-2013-2012.
URL http://www.atmos-meas-tech.net/5/2013/2012/

[12] H. Yatsuzuka, Y. Uetani, Measurement of the all sky spectral radiance distribution using a digital camera with a fisheye lens, J. Environ. Eng., AIJ 78 (690) (2013) 623–629, japanese. doi:10.3130/aije.78.623.

[13] K. Tohsing, M. Schrempf, S. Riechelmann, H. Schilke, G. Seckmeyer, Measuring high-resolution sky luminance distributions with a CCD camera, Appl. Opt. 52 (8) (2013) 1564–1573. doi:10.1364/AO.52.001564.
URL http://ao.osa.org/abstract.cfm?URI=ao-52-8-1564

[14] T. Schmidt, J. Kalisch, E. Lorenz, D. Heinemann, Retrieval of direct and diffuse irradiance with the use of hemispheric sky images, in: International Conference on Energy & Meteorology 2015, Boulder, CO, 2015.
URL http://icem2015.org/resources/oral-presentations/

[15] C. Gauchet, P. Blanc, B. Espinar, B. Charbonnier, D. Demengel, Surface solar irradiance estimation with low-cost fish-eye camera, in: Workshop on "Remote Sensing Measurements for Renewable Energy", Risoe, Denmark, 2012.
URL https://hal-mines-paristech.archives-ouvertes.fr/hal-00741620

[16] B. Urquhart, B. Kurtz, E. Dahlin, M. Ghonima, J. E. Shields, J. Kleissl, Development of a sky imaging system for short-term solar power forecasting, Atmospheric Measurement Techniques 8 (2) (2015) 875–890. doi:10.5194/amt-8-875-2015.
URL http://www.atmos-meas-tech.net/8/875/2015/

[17] Allied Vision Technologies GmbH, Allied Vision Prosilica GE Technical Manual, accessed: 2016-04-11 (Mar. 2015).
URL https://www.alliedvision.com/fileadmin/content/documents/products/cameras/Prosilica_GE/techman/Prosilica_GE_TechMan.pdf

[18] Eastman Kodak Company, KODAK WRATTEN 2 Optical Neutral Density No. 96 Filter / 3.0, accessed: 2016-04-11.
URL http://motion.kodak.com/KodakGCG/uploadedfiles/motion/Kodak/motion/Products/Lab_And_Post_Production/Kodak_Filters/W96-3-0ND.pdf

[19] LI-COR, Inc., LI-200SA Pyranometer Sensor, accessed: 2016-04-11.
URL https://www.licor.com/env/pdf/light/200.pdf

[20] T. Yamada, CCD image sensors, in: J. Nakamura (Ed.), Image Sensors and Signal Processing for Digital Still Cameras, CRC Press, 2005, Ch. 4.

[21] ON Semiconductor, Interline CCD Smear, 2nd Edition, accessed: 2016-04-11 (September 2014).
URL http://www.onsemi.com/pub_link/Collateral/AND9184-D.PDF

[22] B. Urquhart, B. Kurtz, J. Kleissl, Sky camera geometric calibration using solar observations, Atmospheric Measurement Techniques Discussions 2016 (2016) 1–43. doi:10.5194/amt-2015-277.
URL http://www.atmos-meas-tech-discuss.net/amt-2015-277/

[23] PV LIB Toolbox, version 1.2.
URL https://pvpmc.sandia.gov/resources-for-members/pv_lib-toolbox/

[24] R. Perez, P. Ineichen, E. Maxwell, R. Seals, Z. A., Dynamic global-to-direct irradiance conversion models, ASHRAE Transactions - Research Series 98 (1) (1992) 354–369.

[25] R. Perez, S. Kivalov, J. Schlemmer, K. H. Jr., D. Renné, T. E. Hoff, Validation of short and medium term operational solar radiation forecasts in the US, Solar Energy 84 (12) (2010) 2161 – 2172. doi:10.1016/j.solener.2010.08.014.
URL http://www.sciencedirect.com/science/article/pii/S0038092X10002823

[26] H. Yang, B. Kurtz, D. Nguyen, B. Urquhart, C. W. Chow, M. Ghonima, J. Kleissl, Solar irradiance forecasting using a ground-based sky imager developed at UC San Diego, Solar Energy 103 (2014) 502–524. doi:10.1016/j.solener.2014.02.044.
URL http://dx.doi.org/10.1016/j.solener.2014.02.044

[27] R. Chauvin, J. Nou, S. Thil, S. Grieu, Modelling the clear-sky intensity distribution using a sky imager, Solar Energy 119 (0) (2015) 1 – 17. doi:10.1016/j.solener.2015.06.026.
URL http://www.sciencedirect.com/science/article/pii/S0038092X15003345

[28] C. A. Gueymard, Direct and indirect uncertainties in the prediction of tilted irradiance for solar engineering applications, Solar Energy 83 (3) (2009) 432 – 444. doi:10.1016/j.solener.2008.11.004.
URL http://www.sciencedirect.com/science/article/pii/S0038092X08002983